Check for updates

ADVANCED MATERIALS
www.advmat.de

Rapid Drying Principle for High-speed, Pinhole-Less, Uniform Wet Deposition Protocols of Water-Dispersed 2D Materials

Kyeonghun Jeong, Chansoo Kim, Ha Young Lee, Junyi Zhao, Soo-Hyung Choi, Jeong-A Bae, Hyun-Sik Kim, Jeong-Yeon Kim, Youjin Kim, Heechae Choi, Alloyssius E.G. Gorospe, Seung Joon Yoo, Chuan Wang, and Dongwook Lee**

Inexpensive, high-speed deposition techniques that ensure uniformity, scalability, wide applicability, and tunable thickness are crucial for the practical application of 2D materials. In this work, rapid drying is identified as a key mechanism for pioneering two high-speed wet deposition methods: hot dipping and air knife sweeping (AKS). Both techniques allow thickness control proportional to flake concentration, achieving tiled monolayers and pinhole-free coverage across the entire substrate, as long as evaporation outpaces flake diffusion. AKS prevents non-uniformity along substrate edges by eliminating contact line pinning. The achieved deposition speed of 0.21 m^2 min^{-1} with AKS significantly surpasses traditional methods, enabling the equipment for large substrates > 1 m^2. Combined with the ultralow debonding force for mechanically susceptible flexible display production and short-circuit-proof nanometer-thin capacitors with capacitance comparable to commercial multilayer ceramic capacitors (MLCCs), these new protocols showcase simple and swift solutions for manufacturing 2D materials-based nanodevices.

1. Introduction

Since the isolation of graphene in 2004,[1] promising electronic, optical, magnetic, electrochemical, ferroelectric, catalytic, and membrane/barrier properties of two-dimensional materials (2D materials) were unveiled. In the way toward practical use of 2D materials, deposition processes remain the key and at the same time, the bottleneck, as it dictates productivity, scalability, economics, and device performance. The current deposition technique developments in 2D materials mainly focus on applications within electronics, especially field-effect transistors, which necessitate multilayered heterostructures characterized by atomic flatness and suppressed adverse defects. However, not all applications of 2D materials necessarily prioritize the defect suppression and atomic flatness. For instance, 2D material-based catalysts including layered double hydroxides (LDHs) for oxygen evolution reaction (OER)[2] and strained-engineered MoS_{2-x} for hydrogen evolution reaction (HER)[3] deliberately seek atomic defects to enhance catalytic activity, presenting requirements that are distinctly contrasting with those of conventional electronics deposition protocols. Furthermore, the inherent nanoscale thickness of 2D materials has been exploited in solid-state capacitors for higher areal capacitance, where high-quality deposition techniques such as chemical vapor deposition (CVD) can be

K. Jeong, H. Y. Lee, Y. Kim, A. E. Gorospe, D. Lee
Department of Materials Science and Engineering
Hongik University
Seoul 04066, Republic of Korea
E-mail: dongwook@hongik.ac.kr

C. Kim, C. Wang
Institute of Materials Science and Engineering
Washington University in St. Louis
St. Louis, MO 63130, USA
E-mail: chuanwang@wustl.edu

The ORCID identification number(s) for the author(s) of this article can be found under https://doi.org/10.1002/adma.202411447

© 2025 The Author(s). Advanced Materials published by Wiley-VCH GmbH. This is an open access article under the terms of the Creative Commons Attribution License, which permits use, distribution and reproduction in any medium, provided the original work is properly cited.

[Correction added on April 15, 2025, after first online publication: The copyright line was changed.]

DOI: 10.1002/adma.202411447

C. Kim, J. Zhao, C. Wang
Department of Electrical & Systems Engineering
Washington University in St. Louis
St. Louis, MO 63130, USA

S.-H. Choi, J.-A Bae
Department of Chemical Engineering
Hongik University
Seoul 04066, Republic of Korea

H.-S. Kim, J.-Y. Kim
Department of Materials Science and Engineering
University of Seoul
Seoul 02504, Republic of Korea

H. Choi
Department of Chemistry
Xi'an Jiaotong-Liverpool University
Suzhou 215123, P. R. China

S. J. Yoo
School of Materials Science and Engineering
Gwangju Institute of Science and Technology
Gwangju 61005, Republic of Korea

technically challenging and economically undesirable for ferroelectric and electrode oxide 2D materials.[4] Thus, high priority yet still latent demands for 2D material devices that do not require atomic flatness and strict defect suppression can be represented by other requirements: cost-effectiveness, high production speed, scalability to large area with film uniformity, and wide applicability on 2D material/substrate combinations.

In response to those latent needs, wet deposition processes for 2D material devices have been developed to offer simple, cost-effective, and scalable production methods.[5] However, simultaneous fulfillment on high-speed, scalability to large area, broad applicability, and film uniformity requirements by a single wet deposition technique and corresponding design principle is yet to be discovered. Existing wet deposition techniques include spin-casting,[4,6–8] dropcasting,[9] Langmuir–Blodgett assembly,[10,11] Landau-Levich deposition,[12] and electrostatic layer-by-layer assembly;[13,14] although the latter four techniques commonly suffer from sluggish productivity and subsequently limited scalability, along with specificity in solvent/2D materials chemistry, compromising scope of applications (Tables S1 and S2, Supporting Information). Spin-casting shows fast deposition speed yet bares limitation on scalability beyond wafer-scale owing to its own key mechanism: centripetal force mechanically breaking the substrate. Broadly applicable wet deposition processes nondiscriminatory to chemistry of the 2D material/substrate combinations, and processibility on/beyond wafer-scale within minute timeframe can attract demands from underrepresented multiple applications of 2D materials.

In this work, we shed light on rapid drying concepts to uniformly deposit water-dispersible 2D material flakes with 0.21 m^2 min^{-1} deposition speed. The key mechanism is rapid drying, where it simultaneously constrains time for film inhomogeneity-incurring flow and reduces diffusional mobility by instantaneously increased concentration, leaving the 2D material flakes to be homogeneously stacked on the substrates. The rapid drying leads to rapid deposition speed. Exfoliated negatively charged graphene oxide (nGO) and exfoliated montmorillonite (MMT) were selected for their water dispersibility, high-yield exfoliation to monolayers, and hydrophilic nature, aligning with environmental and human health considerations. MMT and nGO flakes dispersed in water are spread as liquid film and then rapidly dried by heating (hot dipping) or air flow (air knife sweeping; AKS) on SiO_2 glass, indium tin oxide (ITO), and single-crystalline Si wafer substrates to demonstrate versatile applicability. These two different drying protocols commonly lead to thin films free from coffee-ring inhomogeneities and pinholes, confirming efficacy of the shared rapid drying principle. The thickness of the deposited thin films is linearly proportional to the flake concentration between monolayers and few-layers, concomitant to the drying mechanism. For both nGO and MMT aqueous dispersions, ≈100% surface coverage is achieved only when the rapid drying principle is abided such that the temperature is above 40 °C or the air flow speed is optimized. Leveraging no limitation in scale-up in this principle, wet deposition equipment for > 1 m^2 substrates has also been constructed. Adjustment of the substrate hydrophobicity by naphthalene masking enables area-selective deposition (ASD) of the water-dispersible 2D material flakes. This scalable quick wet deposition technique demonstrated pinhole-free features over the entire film by low-adhesion debonding layer for flexible display mass production, and nm-thin solid-state capacitors.

2. Results and Discussion

The key hypothesis is that rapid drying can enable rapid solvent (in this work, water except for comparative cases in Figure S7, Supporting Information) removal by which diffusional motion of dispersed flakes is arrested, leading to uniform wet deposition of the water-dispersible 2D material flakes down to atomic monolayers in a short time (Figure S1, Supporting Information). This approach is justified by previous works, which utilized vacuum filtration to fabricate freestanding membranes solely consisting of 2D material flake building blocks.[15,16] As the vacuum filtration quickly removes the solvent, diffusional mobility of the flakes in the dispersion is immediately curtailed, thereby allowing self-assembly into freestanding membranes with lamellar arrangements. However, this manufacturing strategy, which requires porous filters rather than a pore-less substrate, has not been proven to produce thinner films down to monolayers.

Still inspired by this mechanism, alternative strategies involving rapid solvent removal can be devised for thin film deposition via evaporation. Another previous example that demonstrates the potential of rapid drying is spin-casting.[6,8] Although the air flow speed profile varies proportionally to the radial position, the thickness of the deposited film remains uniform across the surface, except at the edges. By addressing the limitations of this method, such as substrate scalability issues caused by the centripetal force breaking the large-area substrates and inhomogeneities along the edge due to flake condensation accelerated by faster evaporation rates at higher air flow speeds, the approach could become more promising. Such improvement would require the application of a uniformly distributed field of air flow, such as air knife sweeping (AKS). The protocols abiding to the rapid drying principle are designed to minimize non-uniformity in the deposited thin film by accelerating the evaporation time scale, thereby limiting the opportunity for lateral flake diffusion that induces inhomogeneity[17] (Note S1, Figure S1, and Table S3, Supporting Information). Hot dipping scheme, corresponding to rapid drying by heating alone without air blowing (**Figure 1A**), and AKS protocol, air blowing alone without heating, have been used to implement rapid drying independently (Figure 1B). Wet deposition equipment for > 1 m^2 substrates synergizes both hot dipping and AKS for further accelerated evaporation speed (Figure 1C).

2.1. Mechanism and Characteristics of Hot Dipping

Rapid drying principle implemented by hot dipping enables few-layered wet deposition of the selected water-dispersible 2D materials (nGO and MMT) without pinholes and coffee rings on hydrophilic flat substrates (**Figures 2** and S3 and S4 and Movie S1, Supporting Information). In this hot dipping protocol, only the temperature determines the evaporation speed since other factors such as atmospheric pressure, relative humidity, and air

© 2025 The Author(s). Advanced Materials published by Wiley-VCH GmbH

15214095, 2025, 15, Downloaded from https://advanced.onlinelibrary.wiley.com/doi/10.1002/adma.202411447 by Junyi Zhao - Stanford University , Wiley Online Library on [16/05/2026]. See the Terms and Conditions (https://onlinelibrary.wiley.com/terms-and-conditions) on Wiley Online Library for rules of use; OA articles are governed by the applicable Creative Commons License

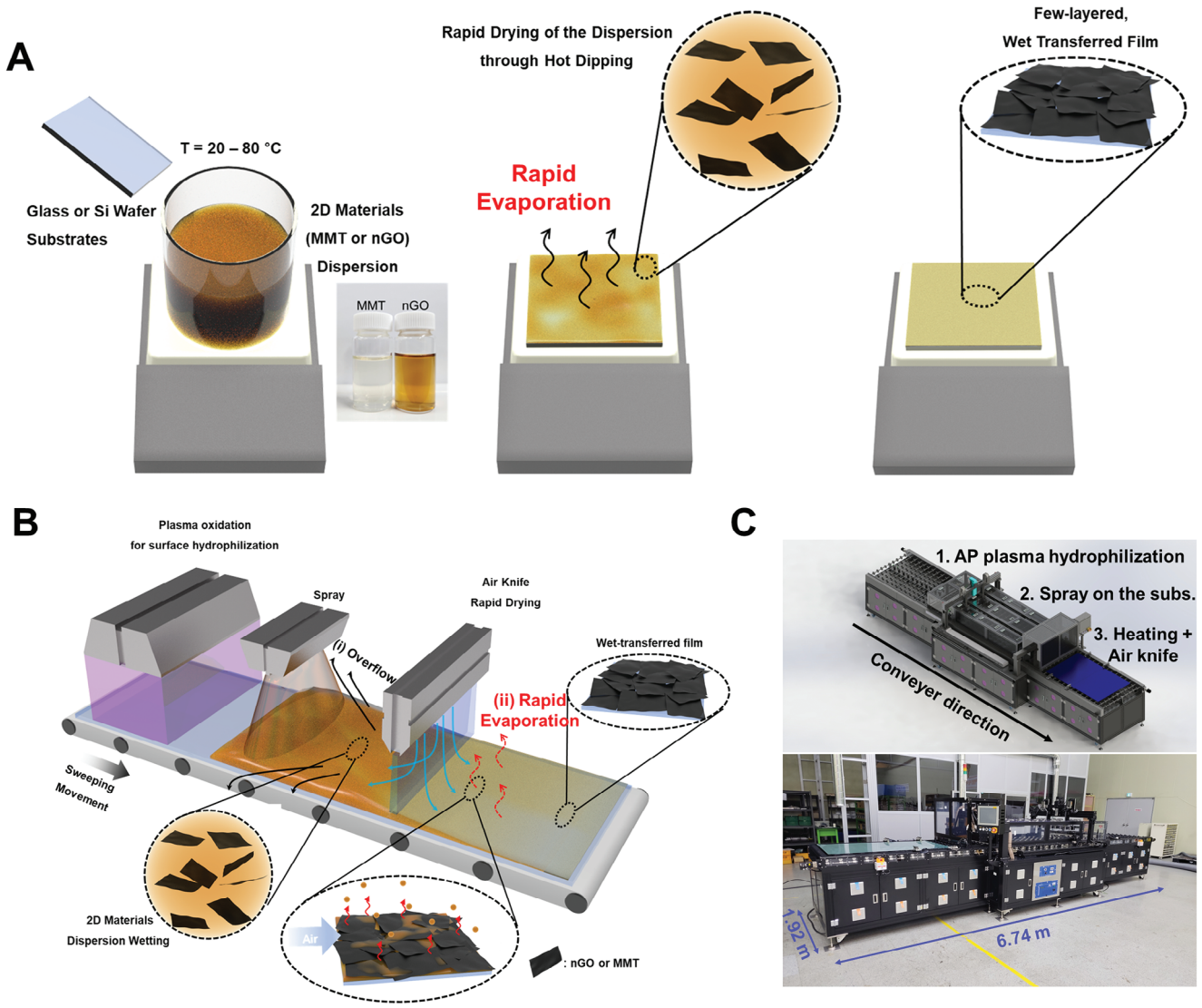

Figure 1. Rapid drying protocols for high-speed, pinhole-less wet deposition of water-dispersible flakes including 2D materials. A) Batch-type hot dipping. The inset photograph shows colorless MMT aqueous dispersion and brownish nGO aqueous dispersion, both at 2.0 g L^{-1} concentration. B) Continuous air knife sweeping (AKS). C) Combination of the hot dipping and AKS to implement rapid drying principle even at large-area deposition.

flow speed are held constant. Elevated temperature with minimal initial liquid film loading by substrate dipping (i.e., to realize the rapid drying, only a small amount of liquid is evaporated) is intentionally introduced to restrict the time for the flakes to flow toward the substrate edge.[18] As designed, hot dipping above 40 °C (i.e., temperature of both the aqueous dispersion and the substrate unified at 60 °C) promotes uniform 2D material-based wet deposition with coverage approaching ≈100% while suppressing coffee rings and pinholes (Figures 2C,D,G,H and S4C,D,H,I,L–N, Supporting Information).[18] Below 40 °C, coffee ring effect, increased roughness, and compromised coverage simultaneously appear[19] (Figures 2A,B,E,F and S4A,B,F,G,J,K, Supporting Information). The convergence of both the surface coverage at ≈100% and roughness below 2.5 nm at 60 °C–80 °C range also suggests a wide processing window. Suppression of the roughness below 2.5 nm despite 60 nm-wide MMT and 135 nm-wide nGO flakes (Table S3, Supporting Information) suggests that the flakes prefer lamellar arrangement, reflecting that flake basal plane-substrate attraction is energetically favored over flake edge – substrate interaction. The disordered stackings in the XRD of both MMT and nGO suggest complete exfoliation down to monolayered flakes deviating from crystalline periodic stacking (Figure S5, Supporting Information),[6,14,20] indicating that even the kinetically fast rapid drying scheme does not shift the lamellar stacking into alternative flake aggregation configuration. The slope in Figures 2J and S3F (Supporting Information) shows the proportionality of film thickness to the flake concentration, indicating that the mechanism solely relies on the evaporation. Formation of thicker 2D material films by simply increasing the concentration is limited to below 10 g L^{-1}, as both MMT and nGO aqueous dispersions form precipitates beyond 10 g L^{-1} (Figure S6, Supporting Information).

© 2025 The Author(s). Advanced Materials published by Wiley-VCH GmbH

15214095, 2025, 15, Downloaded from https://advanced.onlinelibrary.wiley.com/doi/10.1002/adma.202411447 by Junyi Zhao - Stanford University , Wiley Online Library on [16/05/2026]. See the Terms and Conditions (https://onlinelibrary.wiley.com/terms-and-conditions) on Wiley Online Library for rules of use; OA articles are governed by the applicable Creative Commons License

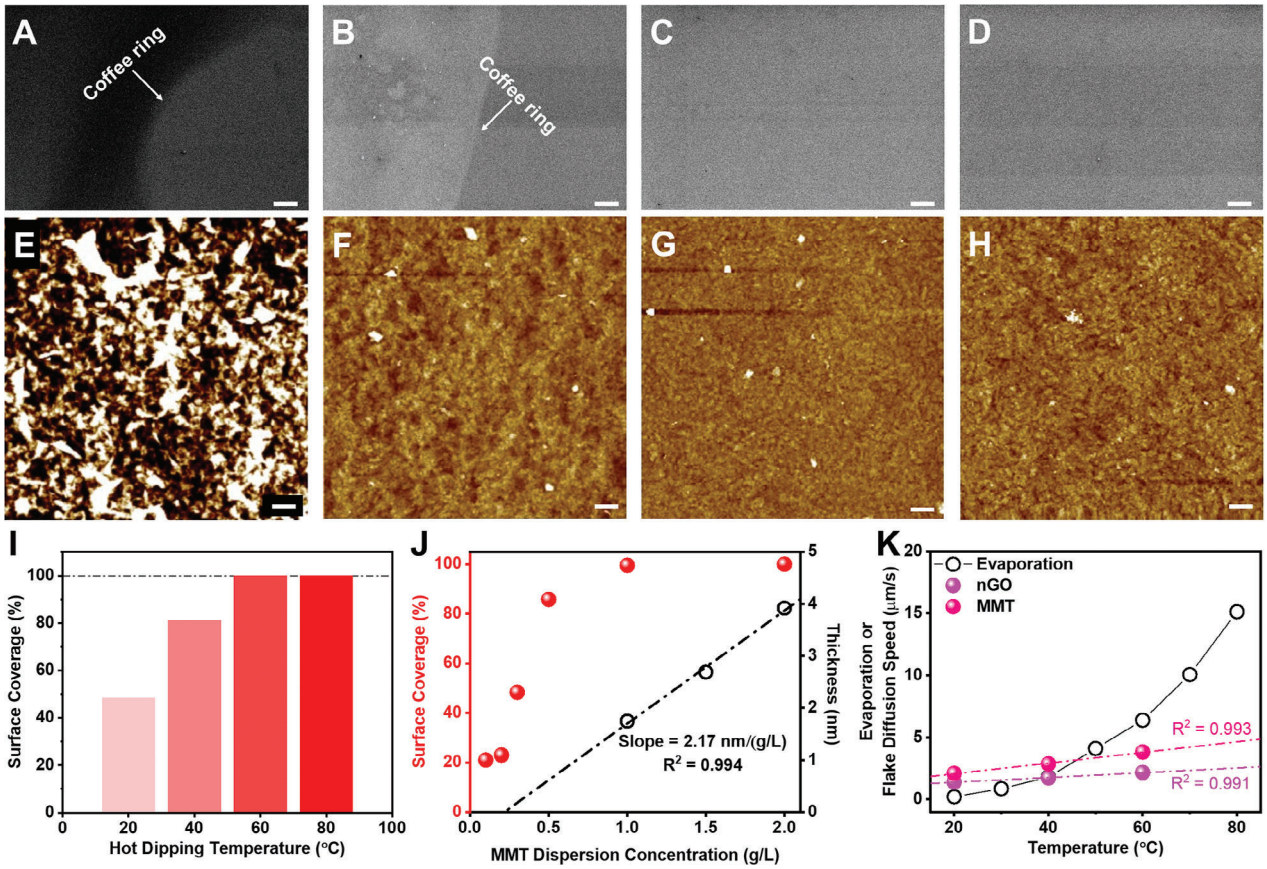

Figure 2. Hot dipping implements the rapid drying principle which can uniformly deposit water-dispersible 2D material flakes on hydrophilic substrates with ≈100% coverage. Schematic of the hot dipping process is introduced in Figure 1A. SEM and AFM images of 2.0 g L^{-1} MMT aqueous dispersion dried on plasma-treated Si wafers under (A) 20 °C, (B) 40 °C, (C) 60 °C, (D) 80 °C substrate and dispersion temperatures. Arrows in (A,B) correspond to coffee ring spots. All scale bars in A–D) correspond to 10 μm. E–H) AFM images of the same. Root-mean-squared roughness (RMS roughness) is 14.3, 2.62, 1.82, and 2.11 nm, respectively. All scale bars in (E–H) correspond to 1 μm. I) Evolution of surface coverage of the wet deposited MMT film as hot dipping temperature is elevated. J) Coverage falls below 100% upon decreasing the flake concentration below 0.5 g L^{-1}, when the hot dipping temperature is fixed at 80 °C. The film thickness is proportional to the MMT aqueous dispersion concentration. K) Liquid film evaporation speed[18] and the DLS-measured average flake diffusion speed at different temperatures (see Note S1 and Table S3, Supporting Information for details). Similar hot dipping trends are also demonstrated for nGO as well (Figures S3 and S4, Supporting Information). It is remarkable that the convergence of surface coverage toward 100%, elimination of the coffee ring effects, and reduction in film roughness above 40 °C all match with the evaporation speed surpassing the flake diffusion speed for both nGO and MMT above 40 °C.

The liquid film descending speed by evaporation must be faster than that of particle diffusion by diffusional motion for pinhole-free film formation[18] (Figure 2K; Note S1, Figure S1, and Table S3, Supporting Information). Mechanistically, when water evaporation occurs rapidly, only a short period of time is allowed for the dispersed flakes to migrate and cause the coffee ring effect. Instead, they are captured in place. Beyond 40 °C, the liquid film descending speed becomes faster than the flake diffusion speed (Figure 2K; Note S1, Figure S1, and Table S3, Supporting Information), which matches well with the temperature range for uniform deposition (Figures 2C,D,G,H and S4C,D,H,I,L–N, Supporting Information). Moreover, systematic shifts in solvent boiling points lead to corresponding shifts in the hot dipping temperatures above which uniform films begin to appear (Figures S1 and S7, Supporting Information), corroborating the criterion for the rapid drying principle again. The temperature drop during the hot dipping remains consistently less than ≈10 °C across the 20 °C–80 °C range (Movie S2, Supporting Information), effectively precluding thermal gradient-driven secondary flows as a latent source of film inhomogeneity.

Despite elimination of coffee ring effects, contact line pinning was unavoidable regardless of the hot dipping temperature, compromising the film uniformity (Movie S2, Supporting Information). Hence, another protocol that further facilitates evaporation speed along with constantly moving contact line was introduced: rapid drying by air flow. This process by air flow can also independently cross-examine whether the ≈100% surface coverage, film smoothness, absence of coffee rings, and the thickness predictability are innate characteristics of protocols abiding to the rapid drying principle or the hot dipping protocol alone. In terms of performance, drying by air flow brings other possibly beneficial features, such as continuous processing completely lifting substrate size restriction for scalability and accelerated deposition speed, if executed on a conveyer stage.

© 2025 The Author(s). Advanced Materials published by Wiley-VCH GmbH

15214095, 2025, 15, Downloaded from https://advanced.onlinelibrary.wiley.com/doi/10.1002/adma.202411447 by Junyi Zhao - Stanford University , Wiley Online Library on [16/05/2026]. See the Terms and Conditions (https://onlinelibrary.wiley.com/terms-and-conditions) on Wiley Online Library for rules of use; OA articles are governed by the applicable Creative Commons License

2.2. Mechanism and Features of Air Knife Sweeping (AKS)

An air knife is a continuous, industrially scalable rapid drying technique with controllable parameters such as conveyer speed and air flow speed where air flow displaces vapor from the air/liquid interface[21] (Figure 1B). The air flow by AKS has uniform air flow speed over all horizontal positions of the substrate and performs two functions. First, the initially loaded liquid film on the substrate is thinned by overflowing portion of the liquid film out of the substrate, thereby decreasing the effective loading of the liquid film. This phenomenon in turn expedites the time for complete drying by lessening the amount of liquid that needs to be dried, critical to realize the rapid drying principle. However, it bears the risk of overthinning the liquid film where effective flake loading is overly disposed by excessive overflow (Figure S8, Supporting Information); in this case, the flake-based thin films can contain pinholes due to insufficient remnant flake loading. Second, air flow accelerates the evaporation of the remnant liquid film by continuously blowing away the water vapor from the air/liquid interface (Figure 1B). The risk at this second stage is weak air flow speed and/or short exposure time to the air flow, where the air flow may fail to dry the liquid film completely; in this circumstance, undried liquid film remains corresponding to underperforming regime, as outlined in Figure S8 (Supporting Information).

Tunable thickness down to monolayer while keeping the surface coverage at ≈100% is achieved over the entire substrate area by optimizing the flake concentration within 0.5–2.0 g L^{-1} range (**Figure 3**A–F). Overlapped tiling among the flakes is observed beyond the monolayer deposition regime due to their arbitrary geometry of the flakes (Figure 3). Additionally, an abrupt drop in surface coverage below certain aqueous dispersion concentrations was observed (Figure 3G), as in the case of hot dipping (Figure 2J). The deposition characteristics are consistent for both nGO and MMT flakes, hinting the wide applicability of the AKS technique for water-dispersible 2D material flakes (Figures 3 and S8 and S9, Supporting Information).

The linearity between flake concentration and the resultant film thickness (Figure 3H) once again manifests that drying is the key driving mechanism in AKS. Under fixed initial liquid film loading, air flow speed and conveyor speed, the first role of AKS, liquid film thinning, is kept consistent. As the residual loading of the aqueous dispersion equalizes and dries thereafter, similar to hot dipping, the resultant film thickness theoretically equals to the effective loading of the liquid film multiplied by the flake concentration. Hence, the average thin film thickness is theoretically expected and experimentally verified proportional to the flake concentration (Figure 3H), achieving tiled monolayers at 2.0 and 0.7 g L^{-1} for MMT and nGO respectively (Figure 3B,E). The speed comparison demonstrates that flake diffusion in aqueous dispersion is rapidly halted by the far faster evaporation speed, a key mechanism shared with the hot dipping protocol for film homogeneities in AKS as well (Figure 3I; Note S1, and Table S3, Supporting Information). Additionally, evaporation increases dispersion concentration and viscosity in both AKS and hot dipping, further reducing flake diffusion speeds as both rapid drying protocols progress. This ensures the flake diffusion speed never outpaces the evaporation speed, confirming robustness of the rapid drying protocols. Distinct from the hot dipping, contact line pinning was not observed for any AKS conditions, as consistent air flow profile and the conveyer constantly moves the contact line (Movies S3 and S4, Supporting Information). The temperature decrement during AKS remains consistently under 5 °C over the entire operating conditions (Movie S4, Supporting Information), ruling out temperature gradient-driven flows as a potential cause of film inhomogeneity.

≈100% coverage and low roughness of nGO and MMT thin films is achieved by the balance between air flow speed and conveyor speed (**Figures** 4A and S8, Supporting Information). When MMT and nGO flakes are wet deposited under a high conveyor speed and low air flow speed, the aqueous dispersion does not dry completely (underperforming). On the contrary, in cases where the overflow of the initially loaded aqueous dispersion is excessive (i.e., when the air flow speed is sufficiently high and the conveyor speed is low), the resultant diminished loading lacks sufficient flakes to cover 100% of the substrate surface, leading to a significant compromise in the film coverage (liquid film overthinning). ≈100% coverage of the nGO and MMT flakes is achieved under multiple air flow speed and conveyer speed combinations, demonstrating wide tolerance of the operational window (Figures 4B and S8, Supporting Information). Even the highest conveyor speed of 3.50 m min^{-1} yields ≈100% surface coverage under 9.3 m s^{-1} air flow speed, demonstrating high productivity reaching 0.21 m^2 min^{-1} wet deposition speed (Figures 4C,D and S8, Supporting Information). The "optimal zone" (≈100% film coverage) occurs only when two steps of the AKS function neither excessively nor insufficiently: i) the loaded aqueous dispersion is reduced, limiting the amount of water that must be evaporated within few seconds, ii) air flow quickly removes water vapor from the otherwise saturated air/liquid interface. A comparison of "optimal" AKS conditions for MMT (Figure 4B) and nGO (Figure S8, Supporting Information) shows that higher viscosity of the nGO aqueous dispersion (as evidenced by the slower diffusivity of nGO presented in Table S3, Supporting Information) limits "overflow" at low air flow speeds, causing incomplete drying (underperforming). Instead at higher air flow speeds (14.1–18.0 m s^{-1}), this viscosity prevents excessive overflow thus inhibiting "overperforming", enabling the stable wet deposition of nGO. In typical industrial settings, the AKS is employed where both conveyor speeds and air flow speeds surpass a few m/s, primarily designed for the cleaning of dust or water from the substrates.[25] Hence, it is natural that the ideal conditions for such wet deposition have remained undiscovered thus far since the conventional AKS operating conditions to dry-clean particulates from substrates belong to the overthinning regime (Figure 4E,F).

The uniformity in both surface coverage and height profiles of MMT and nGO thin films on the SiO_2 glass substrate was confirmed in 9 different spots, even when the conveyer speed is the fastest at 3.50 m min^{-1} (Figures 4G–J and S9, Supporting Information). Among these, 8 spots are located 5 mm from the substrate perimeter, demonstrating negligible edge-induced inhomogeneity in the deposited thin film (Figures 4H–J and S9B–E, Supporting Information), proving that contact line pinning and edge-induced film non-uniformity are overcome. This also constitutes a sharp contrast with a comparable wet deposition technique, such as spin-casting, where 15-mm radius Si

© 2025 The Author(s). Advanced Materials published by Wiley-VCH GmbH

15214095, 2025, 15, Downloaded from https://advanced.onlinelibrary.wiley.com/doi/10.1002/adma.202411447 by Junyi Zhao - Stanford University , Wiley Online Library on [16/05/2026]. See the Terms and Conditions (https://onlinelibrary.wiley.com/terms-and-conditions) on Wiley Online Library for rules of use; OA articles are governed by the applicable Creative Commons License

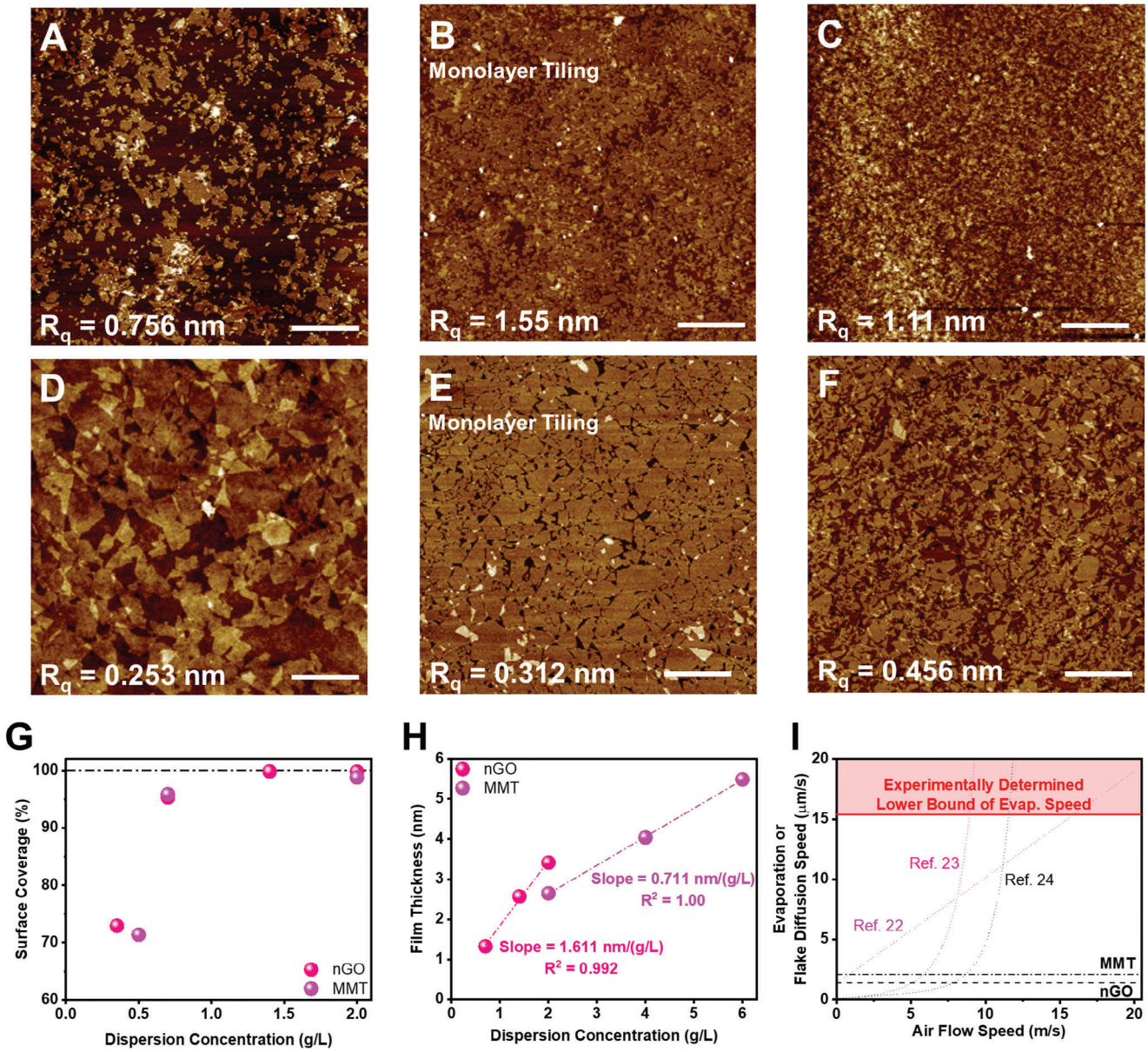

Figure 3. The rapid drying principle through AKS can uniformly deposit 2D material flakes down to monolayer on hydrophilic substrates with ≈100% coverage. AFM images of air knife coated MMT film from the aqueous dispersion concentration of A) 1.0 g L^{-1}, B) 2.0 g L^{-1} (monolayer), C) 3.0 g L^{-1}. AFM images of air knife coated nGO film from the aqueous dispersion concentration of D) 0.5 g L^{-1}, E) 0.7 g L^{-1} (monolayer), F) 2.0 g L^{-1} respectively. The conveyer speed and air flow speed from the air knife were fixed at 3.50 m min^{-1} and 9.3 m s^{-1} respectively. All scale bars in the AFM images correspond to 2 μm. The RMS roughness values are shown in the bottom-left corner of each AFM image. G) Surface coverage as a function of aqueous dispersion concentration. H) Thickness of the wet deposited films are proportional to the flake concentrations. Only the ≈100% surface coverage datapoints were selected here; thus, all the measured films consist of few layered, restacked flakes. I) Comparison of liquid film evaporation speed by AKS and average MMT and nGO flake diffusion speed both at 20 °C (black dashed lines; see Figure S2, Supporting Information for details). Liquid film evaporation exceeding the flake diffusion speed is essential for achieving uniform wet deposition via AKS. The bold flat red line at the top denotes the experimentally established lower limit of the evaporation speed by AKS (15.4 μm s^{-1}; Note S1, Supporting Information), while water liquid film evaporation speed as functions of air flow speed (dotted curves) was modeled using empirical relations adapted from.[22–24]

wafers showed irregularities within 5 mm from the substrate circumference.[8] The height profiles (Figures 4H and S9B, Supporting Information) manifest disordered stacking of the 2D flakes without stepwise increments, consistent with Figure S5 (Supporting Information). Under the 100% coverage condition, AKS demonstrates 2–4 orders of magnitude faster deposition rate (0.21 m^2 min^{-1}) and 1–2 orders of magnitude greater deposition area (i.e., 6-inch Si wafer in Movie S3, Supporting Information) compared to conventional wet deposition techniques (Figure 4K; Table S2, Supporting Information).

A wholistic comparison between the experimentally determined evaporation and flake diffusion speeds (Note S1 and

© 2025 The Author(s). Advanced Materials published by Wiley-VCH GmbH

15214095, 2025, 15, Downloaded from https://advanced.onlinelibrary.wiley.com/doi/10.1002/adma.202411447 by Junyi Zhao - Stanford University , Wiley Online Library on [16/05/2026]. See the Terms and Conditions (https://onlinelibrary.wiley.com/terms-and-conditions) on Wiley Online Library for rules of use; OA articles are governed by the applicable Creative Commons License

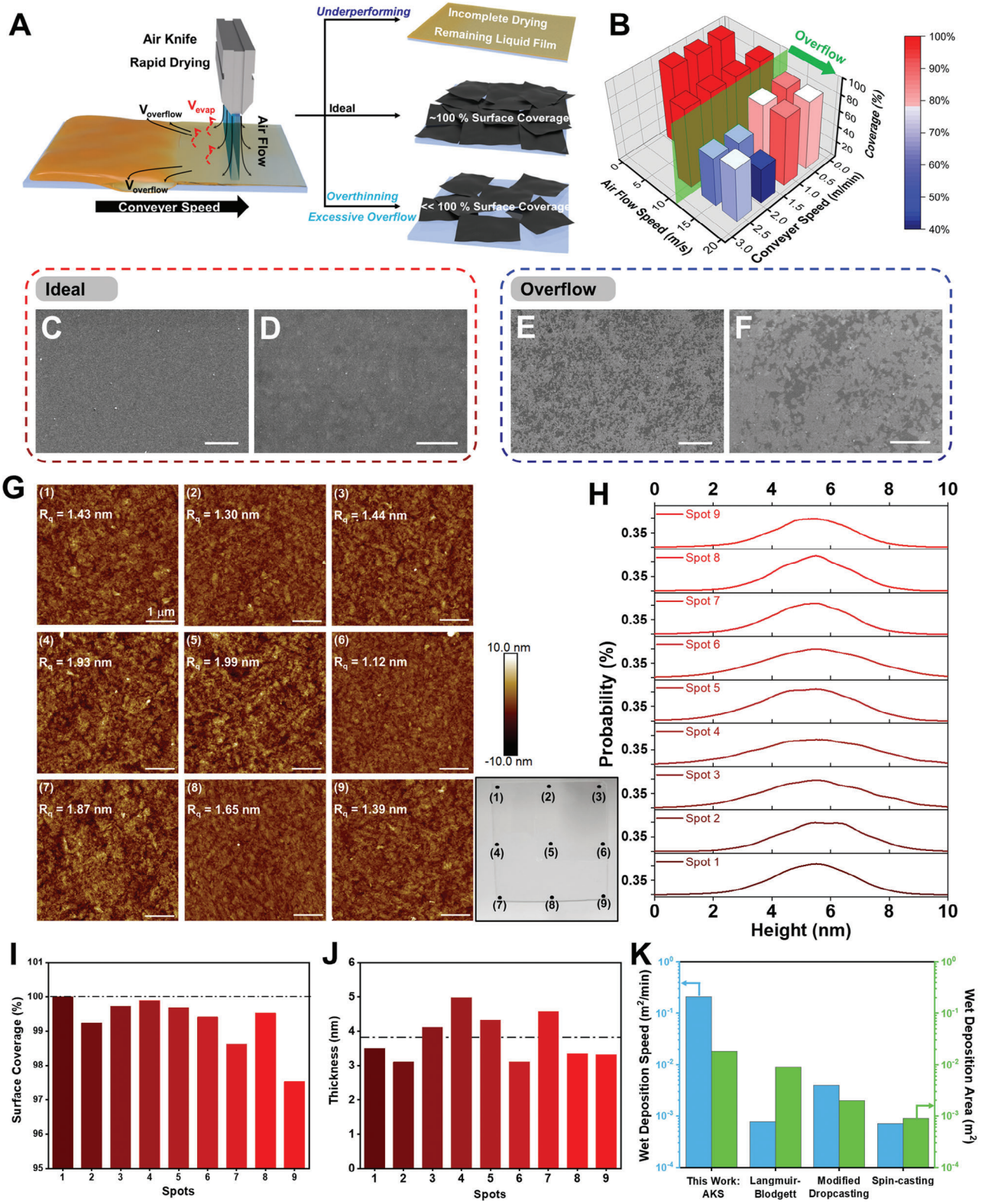

Figure 4. Position-independent wet deposited MMT film uniformity by the AKS even at the proximity with the edges. A) Schematic interpretation of underperforming regime with incomplete liquid film drying and liquid film overthinning regime with excessive liquid film overflow reducing the effective flake loading. B) The range for the ≈100% wet deposition coverage. C) and D) SEM image under the "ideal" wet deposition condition (Scale bars = 4 μm). E) and F) SEM images of insufficient wet deposition coverage due to insufficient effective loading of the aqueous dispersion (Scale bars = 1 μm). G) AFM images of multiple spots of MMT thin film wet deposited to a SiO_2 glass substrate and H) corresponding height profiles. The height

© 2025 The Author(s). Advanced Materials published by Wiley-VCH GmbH

15214095, 2025, 15, Downloaded from https://advanced.onlinelibrary.wiley.com/doi/10.1002/adma.202411447 by Junyi Zhao - Stanford University , Wiley Online Library on [16/05/2026]. See the Terms and Conditions (https://onlinelibrary.wiley.com/terms-and-conditions) on Wiley Online Library for rules of use; OA articles are governed by the applicable Creative Commons License

Table S3, Supporting Information) cross-verifies that validity of the rapid drying criterion for high-quality film deposition: evaporation speed > diffusion speed. Fulfillment of this criterion consistently results in the formation of high-quality films characterized by i) position-independent coating profiles (Figures 4 and S9, Supporting Information), ii) uniform surface coverage (Figures 2–4 and S3,S4,S8,S9, Supporting Information), and iii) minimal film roughness (Figures 2–4 and S3,S4,S8,S9, Supporting Information). This condition was observed at 60 °C and 80 °C for the hot dipping (Figure 2) and at all examined air flow speeds for the AKS system (Figures 3I and S8, Supporting Information). In contrast, when the criterion was not satisfied (i.e., evaporation speed < diffusion speed), the same quality indicators were low, as demonstrated at 20 °C and 40 °C for the hot dipping (Figure 2).

As a cross-validation, systematic adjustments to the solvent boiling point through the addition of water-miscible organic solvents to the aqueous dispersions caused corresponding shifts in the hot dipping temperature at which high-quality coatings first emerged. Specifically, reducing the boiling point by introducing ethanol enabled uniform deposition by the hot dipping without coffee rings even at temperatures as low as 20 °C, whereas increasing the boiling point by incorporating DMSO delayed the onset of such uniform coating formation even beyond 80 °C (Figure S7, Supporting Information).

2.3. ASD Feature by Hydrophobic Mask

Coating a hydrophobic naphthalene mask can realize area-selective deposition (ASD), even on innately hydrophilic SiO_2 glass substrate (Figure S10A, Supporting Information). Naphthalene coating prevents the formation of the uniform liquid film on the coated area by prohibiting wetting by the aqueous dispersion, thereby selectively disabling the wet deposition. Under the process conditions with verified ≈100% coverage (3.50 m min^{-1} of the conveyer speed and 9.3 m s^{-1} of the air flow speed), regions masked with naphthalene show 0% coverage (Figure S10B,D,E, Supporting Information), while the unmasked bare substrate regions keep the ≈100% surface coverage (Figure S10B,C, Supporting Information). This proves that homogeneous wetting is a prerequisite for uniform wet deposition of the water-dispersible 2D material flakes. After the AKS, the naphthalene mask was sublimed in vacuum for its complete removal. No trace of MMT flake residue is left after naphthalene mask sublimation, indicating that the MMT flake was never adsorbed on the naphthalene-masked area (Figure S10D,E, Supporting Information). Reflecting the ≈100% surface coverage only at the unmasked area (Figure S10C, Supporting Information), strong direct bonding between the cured PI and the glass substrate is prevented, lowering the mechanical debonding strength only at the corresponding area (Figure S10F, Supporting Information; vide infra).

2.4. 2–4 Orders of Magnitude Larger Deposition Speed Unlocking Wet Deposition Equipment for > 1 m^2 Substrates

The AKS technique achieves a deposition speed of 2 to 4 orders of magnitude faster than traditional methods (Figure 4K), maintaining film uniformity and compatibility with typical hydrophilic substrates such as ITO, SiO_2 glass, and oxygen-plasma cleaned Si wafers. Additionally, this method avoids the use of harmful organic solvents or additive surfactants, thereby not requiring any specific chemistry (Table S1, Supporting Information).[17,18] The sequential implementation of mutually non-exclusive hot dipping followed by AKS is anticipated to mitigate edge inhomogeneity and accelerate the evaporation process, of which synergistic enhancement in evaporation speed is the key design feature in the > 1 m^2 processible equipment (Figure 1C; Movie S5, Supporting Information).

As industrial applications prefer continuous high-throughput processes with large area scalability, the AKS scheme was upscaled to 1500 × 925 mm^2 sized (half of Gen 6 glass) platform. With the substrate area beyond 1 m^2, the spray-loaded liquid film should be heated before AKS to fully implement the rapid drying principle (Figure 1C); Otherwise, AKS alone cannot completely dry the liquid film particularly at the end of the sweeping scan, thereby falling into underperforming regime (Figure S8, Supporting Information). As such, additional boost in evaporation speed by heating the liquid film is mandated to keep the coverage at ≈100%. Further enhancement in evaporation speed is feasible by AKS on the heated liquid film of the aqueous dispersion, where the latter AKS particularly prevents inhomogeneity-inducing contact line pinning. The > 1 m^2 scale equipment for large-area wet deposition is designed accordingly.

2.5. Pinhole-Less Feature Over Entire Film Toward Applications

Pinhole-less characteristics over the entire film are cross-examined through practical applications of the wet deposited thin films. Initially, trilayered structures consisting of Al thin film / MMT layer / ITO were constructed to ensure 100% surface coverage across the entire substrates (Figure S11, Supporting Information). After mechanically debonding the top Al layer from the trilayered structure, no Al metal surface residue was detected even by a global characterization using XPS (Figure S11, Supporting Information). This finding suggests that the weak van der Waals (vdW) interaction within the lamellar MMT layer (i.e., attraction

profiles indicate uniform deposition of the MMT film even along the edges. Each tick in the y axis represents 0.35% of the probability. Regardless of positions, I) surface coverage and J) film thickness are uniform at ≈100% and 3.10–4.90 nm range. The MMT thin film was wet deposited under the optimized highest production speed condition (i.e., conveyer speed = 3.50 m min^{-1}, air flow speed = 9.3 m s^{-1} from Figure 3) from the 2.0 g L^{-1} MMT aqueous dispersion. All edge spots, (1–9) except spot (5), were 5 mm away from the substrate perimeter. The dashed dot line corresponds to the average thickness. The standard deviations of the surface coverage and the thickness are 0.776% and 0.693 nm, respectively. K) Comparison of wet deposition speed and applicable substrate area among wet deposition techniques. Similar analysis was also performed for nGO films, yielding the same conclusion (Figure S9, Supporting Information).

© 2025 The Author(s). Advanced Materials published by Wiley-VCH GmbH

15214095, 2025, 15, Downloaded from https://advanced.onlinelibrary.wiley.com/doi/10.1002/adma.202411447 by Junyi Zhao - Stanford University , Wiley Online Library on [16/05/2026]. See the Terms and Conditions (https://onlinelibrary.wiley.com/terms-and-conditions) on Wiley Online Library for rules of use; OA articles are governed by the applicable Creative Commons License

between the adsorbed flake to its overlayed one) functions as a sacrificial layer in the mechanical debonding process, as illustrated in **Figures** 5C and S11 (Supporting Information). Also, this strongly proposes the absence of pinholes throughout the entire MMT layer; otherwise, the top Al layers would have been tightly bound to the substrates, leaving torn-off Al residue after the debonding process, as suggested by Figure S11C (Supporting Information). The globally pinhole-less feature fulfills the prerequisites for multiple applications including: i) easily peelable MMT layer replacing the laser liftoff (LLO) process for the mass production of flexible displays (Figures 5 and S12 and Table S4, Supporting Information) and ii) pinhole-free, thus short-circuitless, nm-thin solid-state capacitors (**Figure 6**).

2.6. Mechanical Debonding Layer for Flexible Light Emitting Diode Mass Production

Flexible light-emitting devices, such as foldable displays, are conventionally manufactured on thermally inert polyimide (PI) films. The PI varnish is directly coated and cured on carrier glass substrates to prevent thermal expansion, wrinkling, and possible misalignment during the multilayered device fabrication process. This curing process substantially enhances the bonding force between the glass substrate and the PI film, thus escalating the risks of device damage during subsequent debonding procedures.[26] In industrial mass production settings, the laser liftoff (LLO) technique is typically employed to selectively heat and debond the interface between the PI film and the carrier glass. However, drawbacks of LLO process include i) highly sensitive nanoscale optics alignment, ii) PI surface roughening after LLO causing degraded optical transparency, iii) susceptibility to the particulates on the back side, iv) reduced life span upon repeated bending and folding, v) large capital investments reaching ≈7.5 million USD per equipment. To address these challenges, the high-throughput wet deposition of a 2D material (in this case, MMT) flakes offers an alternative by replacing the LLO process with damage-less mechanical debonding.

Halide perovskites have emerged as promising optoelectronic semiconductors for building next-generation high-performance light-emitting diodes (LEDs) for flexible displays, owing to their exceptional luminescence efficiency and solution processability.[27,28] Thermally inert MMT was selected as the debonding layer constituent over nGO due to its thermal stability (Figure S13, Supporting Information), which is critically required to withstand the PI curing processes peaking at 480 °C. Trapped bubbles between the PI sheet and glass substrate due to the thermal decomposition of the debonding material (e.g., nGO) can lead to misalignment in the subsequent fabrication procedures.

Figure 5A shows the intrinsically flexible perovskite light-emitting diodes (PeLEDs) directly printed on PI substrates. The PeLEDs performed similarly well in terms of brightness and uniformity of electroluminescence (EL), regardless of the inclusion of the debonding layer. However, upon the mechanical peel-off process, the PeLED debonded from the PI / glass bilayered structure experienced severe damage due to local cracking and delamination while the PeLED on the PI / debonding layer / glass trilayered structure remained intact without performance degradation (Figure 5B).

This damage-less debonding process was primarily facilitated by the MMT layer, which impedes direct and strong bonding between the PI sheet and the carrier glass (see Figure S14, Supporting Information for effect of the MMT layer coverage on the debonding force). The MMT debonding layer, deposited under the maximum conveyor speed of 3.50 m min^{-1}, achieves a low debonding force of 1.51 gf/in (1.00 gf/in = 0.386 N m^{-1}). This overachieves the industrial standard of 5 gf/in set by informational display manufacturers (Figure 5C) while also highlighting compatibility with high-throughput mass production owing to its high deposition speed (Figure 4K). In contrast, the debonding force at the direct PI / glass interface without the MMT buffer layer rises to 17.77 gf/in, deviating from the industrial standard. Microscopy analysis (Figure 5D) validates the effectiveness of the MMT layer in preventing micro-cracks in strain-sensitive layers during the debonding process. Moreover, the PeLED peeled off from the PI / MMT / glass trilayered structure demonstrated superior flatness, whereas the one debonded from the PI / glass bilayered structure exhibited severe rolling due to residual strain and plastic deformation of the PI film (Figure 5E,F). The effectiveness of the MMT debonding layer, applicable through high-throughput AKS, represents a viable alternative to conventional LLO processes. It enables cost-effective and high-throughput production of flexible light-emitting devices, eliminating the bottleneck high capital investments and susceptible optical adjustments (Table S4, Supporting Information).

2.7. nm-Thin Solid-State Capacitors

nm-thin capacitor was constructed to reach 10 nm-thick MMT dielectric layer (**Figure 6**A). Capacitance density (areal capacitance; C) is expressed as $C = \epsilon_0 \epsilon_r / d$, where ϵ_0, ϵ_r, d represent vacuum permittivity, dielectric constant of the material, and dielectric layer thickness, respectively. The rationale behind pursuing such nm-thin capacitors lies in the direct correlation between thinner dielectric layers and higher capacitance. Despite the prevalent use of state-of-the-art $BaTiO_3$ material in commercial multilayer ceramic capacitors (MLCCs) down to ≈0.3 µm thickness,[4] further thinning of the $BaTiO_3$ dielectric layer is ineffective by the concurrent reduction in dielectric constant with decreasing particle size, associated with the increasing volume fraction of the less dielectric cubic phase $BaTiO_3$.[30] Moreover, the replacement of conventional sintering process into the rapid drying protocols in the capacitor construction not only boosts productivity but also significantly reduces energy consumption.[31,32]

The nm-thin capacitor exhibits efficient charge storage and minimal leakage current comparable to commercial MLCCs (Figure 6). The absence of short-circuits further confirms the absence of pinholes in the deposited MMT film (Figures 6A and S11D, Supporting Information). Both the leakage currents in the tens of nA range and their insensitivity to DC voltage are shared characteristics between the nm-thin capacitor and MLCCs. Despite the nm-thin capacitor having an active area 2–3 orders of magnitude larger and a dielectric layer thickness an order of magnitude thinner (down to 300 nm for commercial MLCCs[4] vs 10 nm), the leakage current remains comparable, indicating the

© 2025 The Author(s). Advanced Materials published by Wiley-VCH GmbH

15214095, 2025, 15, Downloaded from https://advanced.onlinelibrary.wiley.com/doi/10.1002/adma.202411447 by Junyi Zhao - Stanford University , Wiley Online Library on [16/05/2026]. See the Terms and Conditions (https://onlinelibrary.wiley.com/terms-and-conditions) on Wiley Online Library for rules of use; OA articles are governed by the applicable Creative Commons License

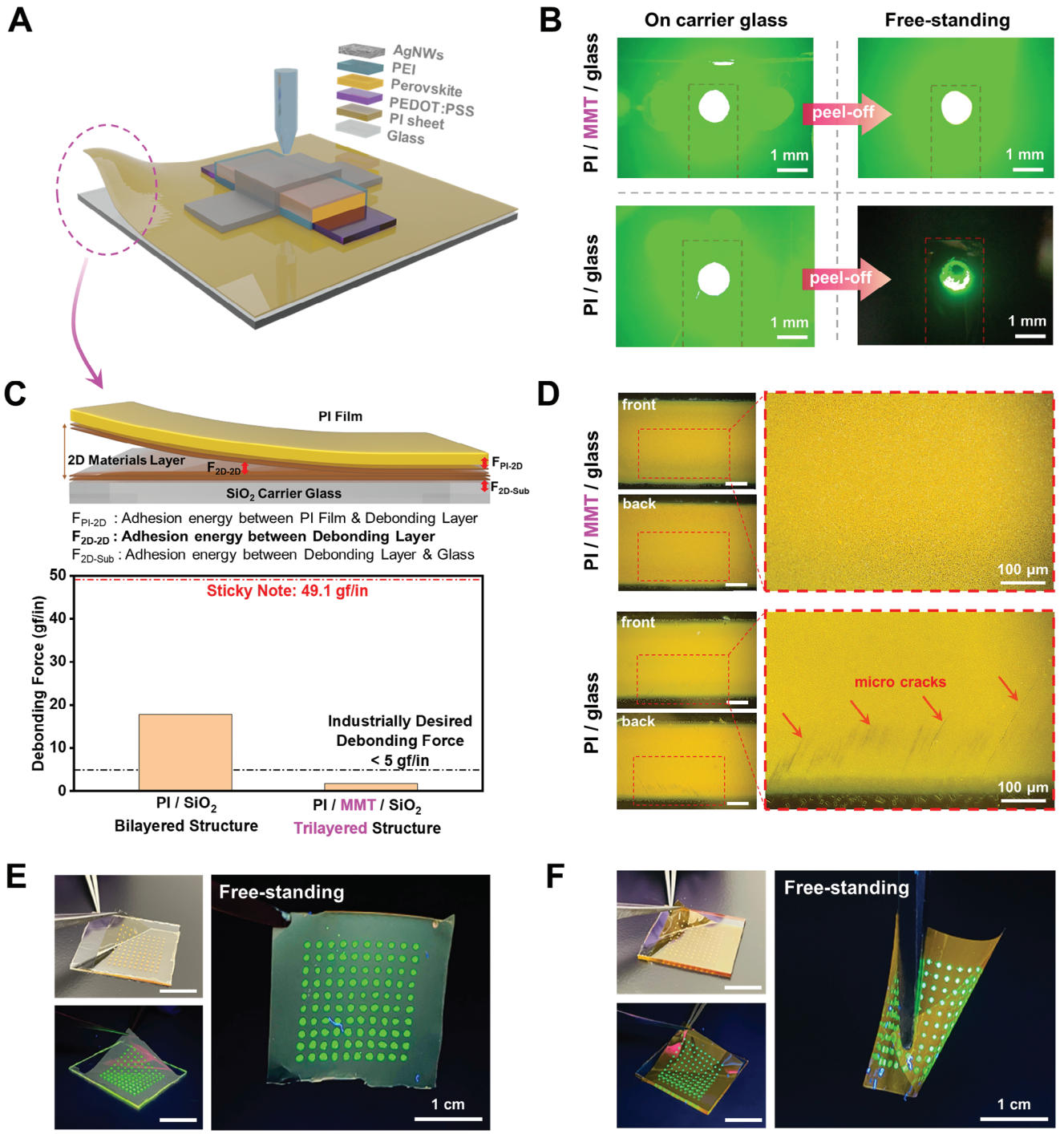

Figure 5. Damage-less mechanical debonding layer deposited through the high-speed AKS for mass production of flexible displays. A) Schematic diagram of the fully inkjet-printed intrinsically flexible PeLEDs on PI sheet. B) Photographs of normally functioning PeLEDs fabricated on PI / MMT / glass and PI / glass multilayered structures before and after mechanical debonding from the glass substrates. C) Scheme of mechanical debonding process for the mass production of flexible light-emitting devices, where the inherent vdW bonding among the wet deposited, lamellar stacked MMT film contributes to small debonding force. Mechanical debonding force (i.e., 180° peel-off force) is significantly dropped by the debonding layer. The black-dashed line represents the safe debonding force set by industrial informational display manufacturers and the red-dashed line provided a reference of debonding force of a sticky note.[29] D) Optical microscopy of the debonded PeLEDs printed on PI / MMT / glass and PI / glass multilayered structures. All scale bars in both the front-view and back-view microscopy images correspond to 200 μm. Photographs of the manual mechanical debonding processes of the fully inkjet-printed perovskite pixels from E) PI / MMT / glass and F) PI / glass multilayered structures, along with the photoluminescence of freestanding perovskite displays under UV illumination.

© 2025 The Author(s). Advanced Materials published by Wiley-VCH GmbH

15214095, 2025, 15, Downloaded from https://advanced.onlinelibrary.wiley.com/doi/10.1002/adma.202411447 by Junyi Zhao - Stanford University , Wiley Online Library on [16/05/2026]. See the Terms and Conditions (https://onlinelibrary.wiley.com/terms-and-conditions) on Wiley Online Library for rules of use; OA articles are governed by the applicable Creative Commons License

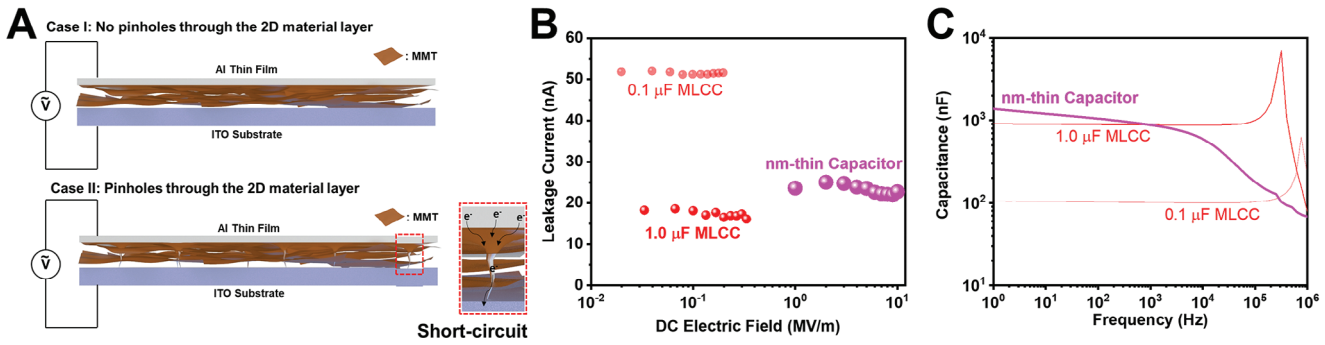

Figure 6. nm-thin solid-state capacitor consisting of a naturally occurring 2D material, MMT. A) Occurrence of short-circuit depends on the existence of pinholes over global scale. B) Leakage current of the Al / 10 nm-thick MMT / ITO trilayered structure constituting the nm-thin capacitor is comparable to those of 2 commercial MLCCs. Each designated DC voltage was sustained for 10 min to measure the average leakage current. Each data point corresponds to a DC voltage ranging from 10 to 100 mV, applied at 10 mV intervals. C) Capacitance of the nm-thin capacitor and the 2 commercial MLCCs as a function of frequency. The abrupt peak of the MLCC capacitances at ≈100 kHz suggests a transition into inductor-like behavior, marking their maximum operatable frequency.

absence of pinholes in the MMT dielectric layer (Figure 6B). In addition, dielectric breakdown was not observed up to 100 mV, corresponding to 10 MV m^{-1} electric field. Along with the large band gap of the exfoliated MMT (3.86 eV),[33] this further corroborates the pinhole-less feature of the MMT layer. The nm-thin capacitor demonstrates capacitance comparable to the 1.0 μF MLCC up to 10 kHz (Figure 6C), positioning it as a cost-effective solid-state capacitor for high-density charge storage upon integration into multilayered or jellyroll-type structures[34] with comparable operating frequencies to the MLCCs. Future developments can focus on substituting MMT with other dielectric 2D materials such as Ti_2NbO_7, $Ca_2Nb_3O_{10}$, and $Ti_{0.87}O_2$ to achieve ultrahigh capacitance.[4]

3. Conclusion

This work has demonstrated the efficacy of the rapid drying principle as a transformative approach for the uniform deposition of water-dispersible 2D material flakes, achieving 2–4 orders of magnitude higher deposition speeds (0.21 m^2 min^{-1}) for > 1 m^2 scalability. When the evaporation is faster than flake diffusion, surface capture occurs, resulting in films with 100% surface coverage without pinholes. By applying the two independent protocols, hot dipping and AKS, the global pinhole-free features, film uniformity and smoothness from rapid drying principles were cross-verified, especially the latter which guarantees higher productivity due to continuous process and position-independent film uniformity owing to the absence of contact line pinning. The wet deposited thickness of the films can be proportionally tuned from monolayer to multilayer through the variation of flake concentration. Despite being a wet process, MMT-based thin films formed through this technology are compatible with high vacuum (Al thin film thermal evaporation), high temperature (PI varnish curing up to 470 °C), and wet post-processes (PI varnish casting on top). This approach is beneficial for multi-field applications such as debonding layers for the mass production of flexible displays and nanometer-thin solid-state capacitors, where high-speed productivity and ≈100% surface coverage are key requirements. These findings also underscore the potential of rapid drying not only to maintain the film quality on hydrophilic 2D material/substrate pairs but also to significantly reduce the time and cost associated with traditional wet deposition protocols.

The simplicity, high-throughput productivity, and large area scalability of these new protocols can enhance economic feasibility for industrial/real-life applications of 2D materials, such as large-area wet-deposition of hydrophilic exfoliated layered double hydroxide (LDH) catalysts for OER.[2] Nevertheless, these methodologies can be, so far, incompatible for heterostructured devices such as field-effect transistors, which require single-crystalline and mm-wide flakes with sub-monolayer roughness. The rapid drying techniques may not be mechanistically limited to 2D materials only, implying that further extension to large-area, high-throughput, uniform deposition of 3D (i.e., microspheres) or 1D (i.e., fibers, nanotubes, or nanorods) particles beyond wafer scale and on curved/flexible substrates remain an open possibility.[18] Furthermore, the rapid drying principle discovered in this work can be alternatively or synergistically implemented by low boiling point solvents (Figure S7, Supporting Information for example) or reduced pressure, thereby opening other complementary high-speed wet deposition protocols in the future.

4. Experimental Section

Aqueous Dispersion of Exfoliated nGO and MMT Monolayered Flakes: Aqueous suspension of nGO was synthesized through a modified Hummers' protocol,[14,20] with sustained reaction temperature down to 5 °C, to avoid defect formation. In brief, the protocol consisted of i) intercalation by H_2SO_4 (Duksan Reagents, 95%), ii) oxidation by $KMnO_4$ (Sigma–Aldrich, 99.0%) iii) hydrolysis for intercalation of water molecules in the galleries, and iv) quenching and washing to produce aqueous dispersion of spontaneously exfoliated and monolayered nGO flakes.

AKS: AKS of the aqueous 2D material (MMT and nGO) dispersion consists of mass production-compatible in-line processes: i) carrier glass or wafer substrates oxidation and cleaning by oxygen plasma, ii) spraying to fully cover the aqueous dispersion in liquid film form on the substrates, then iii) wet deposition of the thin film through rapid drying by air knife.

Before wetting the surface, Si wafer, ITO, and SiO_2 glass substrates were serially washed in sonication bath by acetone (Duksan Reagents, 99.5%), methanol (Duksan Reagents, 99.8%), and distilled water for 10 min, respectively. Then the substrates were treated by oxygen plasma

© 2025 The Author(s). Advanced Materials published by Wiley-VCH GmbH

15214095, 2025, 15, Downloaded from https://advanced.onlinelibrary.wiley.com/doi/10.1002/adma.202411447 by Junyi Zhao - Stanford University , Wiley Online Library on [16/05/2026]. See the Terms and Conditions (https://onlinelibrary.wiley.com/terms-and-conditions) on Wiley Online Library for rules of use; OA articles are governed by the applicable Creative Commons License

(COVANCE-1MP, FemtoScience) at 200 W for 7 min with 10 sccm oxygen flow to eliminate organic contaminants on the substrate surface.

Aqueous dispersions of nGO and MMT were prepared at controlled concentrations and sprayed onto the cleaned substrates by a two-fluid atomizing nozzle (Model YM5JG4, Spraying Systems Korea). Flow rates of the aqueous dispersion and N_2 gas through the nozzle were 3.0 mL min^{-1} and 12.0 L min^{-1}, respectively.

After forming a liquid film with full coverage, air flow is blown by an air knife, fixed 2.0 cm above the substrate. Then the wet substrate is placed on a flat conveyer and moves at controlled constant conveyer speeds ranging from 0.35–3.50 m min^{-1}. The air flow speed from the air knife was monitored on the substrate surface by an anemometer (Model 405i, Testo).

Wet Deposition Equipment for > 1 m^2 Substrates: In brief, this scaled-up equipment depicted at Figure 1C is equivalent to the laboratory-scale AKS equipment, except for only few details. Due to the inability to accommodate a large area substrate in the oxygen plasma chamber, atmospheric plasma (DieHard ND930 Atmospheric Plasma Module, AI KOREA) was adopted instead. Also, a heater for liquid film, absent in the laboratory-scale AKS setup, was installed between the spraying sector and the air knife sector to expedite evaporation speed for the enlarged area.

Damage-Less Mechanical Debonding of Flexible Displays: The mechanical debonding layer was constructed by wet depositing 2.0 g L^{-1} aqueous dispersion of MMT through AKS. Conveyer speed and air flow speed were set at 3.50 m min^{-1} and 9.3 m s^{-1}, respectively (100% surface coverage at Figure 4A). After the wet deposition of MMT on the substrates, polyimide (PI) varnish (PI Advanced Materials) was coated using a film applicator into 12.5 µm thickness. The cast PI varnish was serially cured under vacuum: i) 80 °C for 10 min, ii) 130 °C for 60 min, iii) 175 °C for 60 min, iv) 250 °C for 60 min, and v) 470 °C for 60 min. The ramp rate between succeeding heating steps was fixed at 5 °C min^{-1}.

On the cured PI surface, the flexible PeLED devices were fabricated through a sequence of inkjet printing processes by a micro plotter (Sonoplot Inc.). These PeLEDs featured a well-established multi-layer architecture comprising a poly(3,4-ethylenedioxythiophene):polystyrene sulfonate (PEDOT:PSS) transparent anode, a methylammonium lead tribromide ($MAPbBr_3$) light-emitting layer, a polyethyleneimine (PEI) buffer layer, and silver nanowires (Ag NWs) as top cathode. Detailed information regarding the ink formulation and comprehensive device characterizations can be found in recent publications.[27,28,35] Debonding force measurements of PI films on the MMT debonding layer were performed in a 180° debonding testing configuration (UNITECHTM R&B302-01 Microload).

Construction and Characterization of nm-Thin Solid-State Capacitors: The oxygen-plasma cleaned ITO substrate was hot dipped in a 2.0 g L^{-1} MMT flake aqueous dispersion at 80 °C. Afterward, Al was deposited on the MMT-coated ITO substrates in a thermal evaporator to form 100 nm-thick Al top layer. The working pressure was fixed at 10^{-5} to 10^{-6} Torr range. The deposition rate was initially set to 0.1 nm s^{-1} until a 30 nm-thick Al film was reached, then increased to 1.0 nm s^{-1} for the next 70 nm thickness. Debonding force measurements of Al thin films on the MMT layer were conducted in a 180° debonding testing configuration (UNITECHTM R&B302-01 Microload). Impedfance spectroscopy was used for capacitance density measurements on the nm-thin solid-state capacitors. Under open-circuit condition, 10 mV of AC voltage was scanned over a frequency range of 1.0 MHz–1.0 Hz.

Other Characterizations: The morphology of the wet deposited thin films was observed by field emission scanning electron microscopy with energy dispersive spectroscopy (HITACHI Regulus 8230). The morphology, surface coverage and thicknesses of such films were characterized by atomic force microscopy (AFM; MultiMode 8-HR, Bruker), in accordance with previously established protocols,[36,37] where the invasive thickness measurements involved selective mechanical scratching of the films followed by step height analysis (exemplar details can be found in Figure S15, Supporting Information). The thickness of nGO films was also measured by a non-destructive visible light absorption for cross-verification.[14] Temperature-dependent dynamic light scattering (DLS) measurements were performed using a Nano Particle Analyzer (SZ-100, HORIBA) with a 532 nm diode-pumped solid-state laser. X-ray photoelectron spectroscopy (XPS) was conducted in ThermoFisher K-Alpha XPS System. X-ray diffraction (XRD) characterizations were performed in a D8 Advance X-ray diffractometer (Bruker, Germany) with Cu Kα1 radiation (λ = 0.154059 nm) at a scan rate of 1°/min. Thermogravimetric analysis (TGA) surveyed the thermal stability of nGO and MMT via a STA 449F3-1053-M TGA (Netzsch, Germany) under dry air at a heating rate of 5 °C min^{-1} over a temperature range of 30 °C–600 °C.

Supporting Information

Supporting Information is available from the Wiley Online Library or from the author.

Acknowledgements

This research was supported by the Electronic Component R&D Program through the Korea Evaluation Institute of Industrial Technology (KEIT) funded by the Korean government (MOTIE) (Award Number 20016367). This work was supported by the Technology Innovation Program (RS-2024-00507804, Development of self-controlling system and process analysis equipment for secondary cathode material quality) funded by the Ministry of Trade, Industry & Energy (MOTIE, Korea). Dongwook Lee was also supported by 2025 Hongik University Research Fund. The authors acknowledge valuable discussion with Prof. Hyoungsoo Kim at Korea Advanced Institute of Science and Technology (KAIST). The authors also acknowledge polyimide (PI) varnish donation from PI Advanced Materials. K.J. and C.K. contributed equally to this work.

Conflict of Interest

Kyeonghun Jeong, Ha Young Lee, and Dongwook Lee are authors on two pending patents related to this work by the Korean Intellectual Property Office (Application No. 10-2023-0042718, 31 March 2023; Application No. 10-2023-0173902, 5 December 2023). All other authors declare they have no competing interests.

Data Availability Statement

The data that support the findings of this study are available from the corresponding author upon reasonable request.

Keywords

2D materials, m^2 min^{-1} scale deposition speed, monolayer, pinhole-free, rapid drying principle

Received: August 4, 2024
Revised: January 4, 2025
Published online: February 10, 2025

[1] K. S. Novoselov, A. K. Geim, S. V. Morozov, D. Jiang, Y. Zhang, S. V. Dubonos, I. V. Grigorieva, A. A. Firsov, *Science* **2004**, *306*, 666.
[2] B. Zhang, L. Wang, Z. Cao, S. M. Kozlov, F. P. García de Arquer, C. T. Dinh, J. Li, Z. Wang, X. Zheng, L. Zhang, Y. Wen, O. Voznyy, R. Comin, P. De Luna, T. Regier, W. Bi, E. E. Alp, C.-W. Pao, L. Zheng, Y. Hu, Y. Ji, Y. Li, Y. Zhang, L. Cavallo, H. Peng, E. H. Sargent, *Nat. Catal.* **2020**, *3*, 985.

© 2025 The Author(s). Advanced Materials published by Wiley-VCH GmbH

15214095, 2025, 15, Downloaded from https://advanced.onlinelibrary.wiley.com/doi/10.1002/adma.202411447 by Junyi Zhao - Stanford University , Wiley Online Library on [16/05/2026]. See the Terms and Conditions (https://onlinelibrary.wiley.com/terms-and-conditions) on Wiley Online Library for rules of use; OA articles are governed by the applicable Creative Commons License

[3] D. Rhuy, Y. Lee, J. Y. Kim, C. Kim, Y. Kwon, D. J. Preston, I. S. Kim, T. W. Odom, K. Kang, D. Lee, W.-K. Lee, *Nano Lett.* **2022**, *22*, 5742.
[4] M. S. Khan, H.-J. Kim, Y.-H. Kim, Y. Ebina, W. Sugimoto, T. Sasaki, M. Osada, *Small* **2020**, *16*, 2003485.
[5] S. Pinilla, J. Coelho, K. Li, J. Liu, V. Nicolosi, *Nat. Rev. Mater.* **2022**, *7*, 717.
[6] N. Sakai, T. Sasaki, *Langmuir* **2022**, *38*, 12399.
[7] H. Yano, N. Sakai, Y. Ebina, R. Ma, M. Osada, K. Fujimoto, T. Sasaki, *ACS Appl. Mater. Interfaces* **2021**, *13*, 43258.
[8] K. Matsuba, C. Wang, K. Saruwatari, Y. Uesusuki, K. Akatsuka, M. Osada, Y. Ebina, R. Ma, T. Sasaki, *Sci. Adv.* **2023**, *3*, e1700414.
[9] Y. Shi, M. Osada, Y. Ebina, T. Sasaki, *ACS Nano* **2020**, *14*, 15216.
[10] L. Xu, A. R. Tetreault, H. H. Khaligh, I. A. Goldthorpe, S. D. Wettig, M. A. Pope, *Langmuir* **2019**, *35*, 51.
[11] T. Zhao, R. Wang, L. Li, T. Jiao, *Nano Futures* **2023**, *7*, 022002.
[12] D. Pareek, K. G. Roach, M. A. Gonzalez, L. Büsing, J. Parisi, L. Gütay, S. Schäfer, *Sci. Rep.* **2021**, *11*, 13993.
[13] J. Lipton, G.-M. Weng, J. A. Röhr, H. Wang, A. D. Taylor, *Matter* **2020**, *2*, 1148.
[14] W. J. Lee, C. S. Kim, S. Y. Yang, D. Lee, Y. S. Kim, *Chem. Eng. J.* **2022**, *440*, 135913.
[15] K. Raidongia, J. Huang, *J. Am. Chem. Soc.* **2012**, *134*, 16528.
[16] J. J. Shao, K. Raidongia, A. R. Koltonow, J. Huang, *Nat. Commun.* **2015**, *6*, 7602.
[17] H. Zargartalebi, S. H. Hejazi, A. Sanati-Nezhad, *Nat. Commun.* **2022**, *13*, 3085.
[18] Y. Li, Q. Yang, M. Li, Y. Song, *Sci. Rep.* **2016**, *6*, 24628.
[19] X. Sun, C. Zhu, T. Fu, Y. Ma, H. Z. Li, *Chem. Eng. Sci.* **2018**, *188*, 158.
[20] W. J. Lee, C. S. Kim, S. Y. Yang, D. Lee, Y. S. Kim, *Carbon* **2021**, *182*, 214.
[21] J. Ding, Q. Han, Q. Q. Ge, D. J. Xue, J. Y. Ma, B. Y. Zhao, Y. X. Chen, J. Liu, D. B. Mitzi, J. S. Hu, *Joule* **2019**, *3*, 402.
[22] P. J. Uno, *ACI Mater. J.* **1998**, *95*, 365.
[23] M. T. Pauken, *Exp. Therm. Fluid Sci.* **1998**, *18*, 334.
[24] A. Jodat, M. Moghiman, M. Anbarsooz, *Heat Mass Transfer* **2012**, *48*, 1397.
[25] S. Park, K. Park, *J. Comput. Des. Eng* **2022**, *9*, 1388.
[26] A. Sezer Hicyilmaz, A. C. Bedeloglu, *SN Appl. Sci.* **2021**, *3*, 363.
[27] J. Zhao, L.-W. Lo, Z. Yu, C. Wang, *Nat. Photonics* **2023**, *17*, 964.
[28] J. Zhao, L.-W. Lo, H. Wan, P. Mao, Z. Yu, C. Wang, *Adv. Mater.* **2021**, *33*, 2102095.
[29] H. J. Kim, K. Jin, J. Shim, W. Dean, M. A. Hillmyer, C. J. Ellison, *ACS Sustainable Chem. Eng.* **2020**, *8*, 12036.
[30] T. HOSHINA, *J. Ceram. Soc. Jpn.* **2013**, *121*, 156.
[31] C. C. Lin, W. C. J. Wei, C. Y. Su, C. H. Hsueh, *J. Alloys Compd.* **2009**, *485*, 653.
[32] H. T. Kim, Y. H. Han, *Ceram. Int.* **2004**, *30*, 1719.
[33] K. Peng, H. Wang, X. Li, J. Wang, Z. Cai, L. Su, X. Fan, *Sci. Rep.* **2019**, *9*, 16325.
[34] P. Jain, E. J. Rymaszewski, *Thin-Film Capacitors for Packaged Electronics*, Kluwer Academic Publishers, Norwell, MA, **2004**.
[35] L.-W. Lo, J. Zhao, H. Wan, Y. Wang, S. Chakrabartty, C. Wang, *ACS Appl. Mater. Interfaces* **2021**, *13*, 21693.
[36] D. Lee, S. Y. Sayed, S. Lee, C. A. Kuryak, J. Zhou, G. Chen, Y. Shao-Horn, *Nanoscale* **2016**, *8*, 19754.
[37] D. Lee, J. Zhou, G. Chen, Y. Shao-Horn, *Adv. Electron. Mater.* **2019**, *5*, 1800624.

© 2025 The Author(s). Advanced Materials published by Wiley-VCH GmbH

15214095, 2025, 15, Downloaded from https://advanced.onlinelibrary.wiley.com/doi/10.1002/adma.202411447 by Junyi Zhao - Stanford University , Wiley Online Library on [16/05/2026]. See the Terms and Conditions (https://onlinelibrary.wiley.com/terms-and-conditions) on Wiley Online Library for rules of use; OA articles are governed by the applicable Creative Commons License